

A Radio/Optical Integrated Navigation Method Based on Ephemeris Correction for an Interplanetary Probe to approach a Target Planet

Xin Ma¹, Jiancheng Fang¹, Xiaolin Ning¹, Gang Liu¹ and Hui Ye²

¹(School of Instrumentation Science and Opto-Electronics Engineering, Beihang University (Beijing University of Aeronautics and Astronautics), Beijing 100191, PRC)

²(Shanghai Institution of Satellite Engineering, Shanghai, 200240, PRC)

(E-mail: maxin@buaa.edu.cn)

To obtain accurate navigation results with respect to Earth simultaneously with those with respect to the target for an interplanetary probe to approach the target planet, this paper proposes a Radio/Optical integrated navigation method based on ephemeris correction, which deeply affects the fusion accuracy. In this paper, the model of the ephemeris error is established, and taking the analytical solution of the ephemeris uncertainty as measurement, the target ephemeris error and its covariance are estimated by Kalman filter and fed back to modify the force models. By correcting the target ephemeris and using information fusion, the Radio/Optical integrated navigation prevents the ephemeris uncertainty polluting the fusion accuracy, and efficiently combines the radio and optical navigation results. The results show the influence of the ephemeris error can be removed, and the Radio/Optical integrated navigation is capable of providing accurate navigation results with respect to Earth and the target. The results demonstrate the proposed method yields an accuracy superior to the conventional method, which proves its effectiveness.

KEYWORDS

1. Information fusion.
2. Optical navigation.
3. Radio navigation.
4. Ephemeris error estimation.

Submitted: 13 July 2014. Accepted: 9 October 2015. First published online: 24 November 2015.

1. INTRODUCTION. Space agencies in the world have focused on Solar System exploration. China intends to launch a Mars probe in the near future, which will lead China one step further in interplanetary exploration (Fang and Ning, 2010; Wu et al., 2011; Ma et al., 2013). Launch, Cruise, Approach and Orbit Insertion, and Entry Descent and Landing (EDL) are four major phases in exploring a target; the Approach and Orbit Insertion phase is vital for interplanetary missions because its

accuracy deeply affects the following EDL phase (Wang et al., 2008) and avoiding a fault in navigation is essential to ensure mission success.

Radio navigation and autonomous navigation are used in interplanetary navigation. Radio navigation measures the signal delay time and the frequency shift to obtain the range and range rate from a probe to a Deep Space Network station (Thornton and Border, 2003). Its accuracy with respect to Earth is excellent, and is dominant for interplanetary missions. However, this is restricted to the visible arcs of the station and Sun conjunction, and its performance with respect to the target mainly suffers from target ephemeris uncertainty (Jordan et al., 1972).

Autonomous navigation can obtain the probe position and velocity without Earth tracking, which is currently only a complementary navigation method despite progress. Three autonomous navigation methods have been proposed. Optical navigation (OpNav) finds the centroids from the optical image of the target and its background stars, and calculates the probe position with respect to the target, which has been used in Mars Reconnaissance Orbiter (MRO), Deep Space 1, and Deep Impact, etc (Martin-Mur et al., 2008). Optical Doppler navigation measures the Doppler-shift spectrum of the Sun or stars to determine the probe velocity (Yim et al., 2000; Guo, 1999). X-ray Pulsar navigation compares the measured arrival time of the pulsar signal with predictions to locate the probe, which has been validated in an on-orbit experiment (Graven et al., 2008; Wood et al., 2001). Among these methods, OpNav is the only method which has been successfully utilised in interplanetary missions.

In previous missions, the navigation results have been provided by direct combination without information fusion, using OpNav results for those with respect to the target and radio navigation ones for those with respect to Earth. This is because OpNav is superior in its accuracy with respect to the target and radio navigation can achieve better accuracy with respect to the Earth (Klumpp et al., 1980). However, this method combines information with lower efficiency (Antreasian et al., 2008). To enhance the performance of the Integrated Navigation System (INS) and obtain more accurate results with respect to both Earth and the target, a key technology is information fusion.

However, if data is to be efficiently integrated, coordinate transformations are required to integrate the two navigation results in the same coordinate system, which introduces target ephemeris uncertainty and directly affects the INS accuracy. Therefore, the planetary ephemeris uncertainty is the main reason for the inaccurate fusion results.

A global fit on the ground can give accurate ephemeris results, which has been utilised for ephemeris correction in several interplanetary missions (Rourke et al., 1977; Riedel et al., 1990; Murrow and Jacobson, 1988). However it requires intensive computational time and large memory to store a complicated model, and is usually used in post-flight analysis to improve the ephemeris. An analytical method based on the geometry of the Earth, the probe, and the target is useful for calculating the ephemeris (Rosenblatta et al., 2008), which requires less memory and computation time. However, the calculated ephemeris is not accurate enough and errors still exist in the force model (Ma et al., 2012). Hence an estimation method based on the analytical solution and a simple model of the ephemeris uncertainty could be an attractive method to balance the accuracy and real-time performance.

Since the ephemeris error belongs to system error, the corresponding estimation methods mainly include Least Squares (LS), Kalman Filter (KF) and Neural

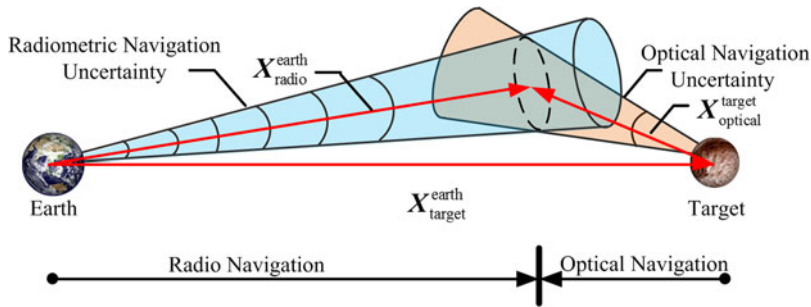


Figure 1. Error Conics for Radio and Optical Navigation.

Networks (NN). LS has the lowest computation cost and needs a large memory to store a batch of measurements and its accuracy depends on the number of measurements (Zhou et al., 1999). KF is an algorithm that recursively estimates the states by the state and measurement models and their noise statistic characteristics (Ning et al., 2012a). NN is an intelligent method using a set of neurons to estimate or approximate the functions or the model, which is especially useful for systems with unknown model and requires larger memory and higher computation capability (Karniely and Siegelmann, 2000). Thus, with regards to the known model of the ephemeris error and the real time requirement, KF is the most suitable method for estimating ephemeris uncertainty.

Ning and Fang (2008) provide an information fusion method for Earth satellites to effectively combine the Doppler and celestial measurements. However, the study ignores the influence of the ephemeris uncertainty. Motivated by Ning and Fang (2008), this paper proposes a Radio/Optical information fusion method based on estimation and correction of the target ephemeris error. The main contribution of this paper is:

- (1) The ephemeris error model is established and by taking the analytical ephemeris uncertainty as measurement the target ephemeris error and its covariance are estimated and fed back to modify the force models.
- (2) Based on the accurate target ephemeris and information fusion, the INS provides precise information with respect to both Earth and the target.

This paper is organised as follows: Section 2 describes a concept of interplanetary navigation and ephemeris correction. Section 3 and Section 4 present the models of the ONS and the RNS. Section 5 presents the analysis of the uncertainties in the force model. Section 6 gives the filter methods, target ephemeris correction, the information fusion algorithms and coordinate transformations. In Section 7, taking Mars as a target, simulations are provided. Finally, Section 8 concludes.

2. A CONCEPT OF INTERPLANETARY NAVIGATION AND ANALYTICAL METHOD FOR EPHEMERIS CORRECTION. Figure 1 shows a concept of interplanetary navigation. As shown in Figure 1, radio navigation accuracy with respect to Earth decreases as the distance between the probe and Earth increases. Unlike radio

Table 1. Ephemeris Accuracy of DE421 in 2008.

Planet	Accuracy
Mercury	A few kilometres
Venus	200 m
Earth	300 m
Mars	300 m
Jupiter	Tens of kilometres
Saturn	Tens of kilometres

navigation, the closer the probe approaches the target, the more precise navigation performance OpNav can provide (Klumpp et al., 1980).

As discussed, the planetary ephemeris is the main reason for the inaccuracy of the INS. Table 1 shows the accuracy of the DE421 ephemeris in 2008 (Folkner et al., 2008). The ephemeris of Venus, Earth, Mars, Jupiter and Saturn is accurate (200 m ~ tens of kilometres), whereas the other planets' ephemeris uncertainties are of the order of thousands of kilometres. Without new observations, DE421 accuracy rapidly decreases. According to Folkner (2010), Mars ephemeris uncertainty declines to about 10 km by the end of 2015, and ephemeris uncertainties of other planets (except the Earth) are even larger by then.

According to the geometry of the probe, target and Earth, the target ephemeris X_{target}^{helio} with respect to the Sun can be determined by optical measurement $X_{optical}^{target}$ and radio measurement X_{radio}^{earth} (Figure 1)

$$X_{target}^{helio} = X_{earth}^{helio} + X_{radio}^{earth} - X_{optical}^{target} \tag{1}$$

where, X_{earth}^{helio} is the Earth vector with respect to the Sun.

By calculating and correcting the ephemeris X_{target}^{helio} using the analytical method, the navigation errors caused by the ephemeris uncertainty can be reduced in the INS.

3. OPTICAL NAVIGATION SUBSYSTEM (ONS)

3.1. *The force model in the ONS.* The ONS force model is established in the Target-Centred Inertial (TCI) coordinate system, taking Mars as a target:

$$\begin{cases} \dot{\mathbf{r}} = \mathbf{v} \\ \ddot{\mathbf{r}} = -\mu_m \frac{\mathbf{r}}{r_{pm}^3} - \mu_s [\frac{\mathbf{r} - \mathbf{r}_s}{r_{ps}^3} + \frac{\mathbf{r}_s}{r_{ms}^3}] - \sum_i^{N(i \neq 4)} \mu_i [\frac{\mathbf{r} - \mathbf{r}_i}{r_{pi}^3} + \frac{\mathbf{r}_i}{r_{mi}^3}] + \mathbf{w} \end{cases} \tag{2}$$

where in the TCI system $\mathbf{r} = [x, y, z]^T$ is the probe position vector, $\mathbf{v} = [v_x, v_y, v_z]^T$ is the probe velocity vector, μ_m, μ_s, μ_i are the gravitational parameters of Mars, Sun, and the i th planet respectively, r_{ps}, r_{pm}, r_{pi} are the distances between the probe and Sun, Mars, and the i th planet respectively, $\mathbf{r}_s = [x_s, y_s, z_s]^T$ are the coordinates of Sun, $\mathbf{r}_i = [x_i, y_i, z_i]^T$ are the position vector of the i th planet, which can be obtained from the ephemeris, and $\mathbf{w} = [w_x, w_y, w_z]^T$ are the process noises in the three-axis velocity.

The force model can be written in the general form:

$$\dot{\mathbf{X}}_1(t) = f_1(\mathbf{X}_1(t), t) + \mathbf{w}_1(t) \tag{3}$$

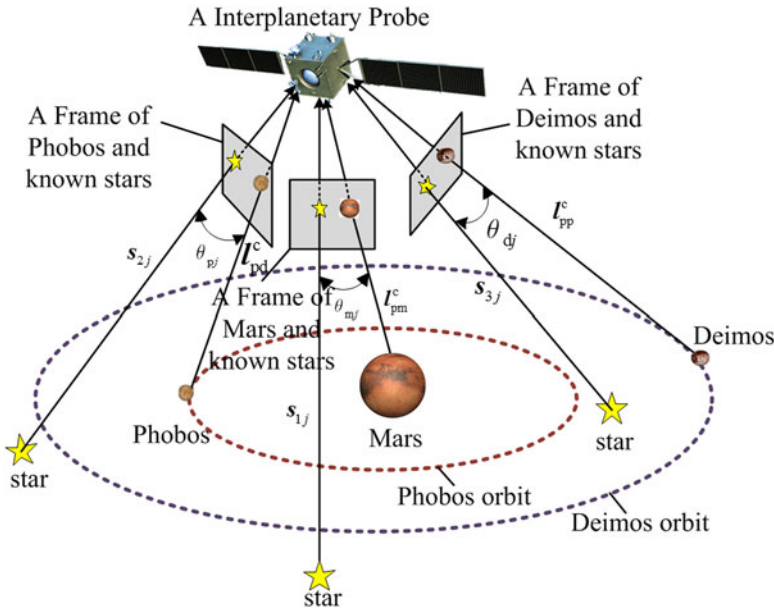


Figure 2. Measurement of ONS.

where $X_1 = [x, y, z, v_x, v_y, v_z]^T$ is the ONS state vector, $f_1(\cdot)$ is the ONS dynamic model function, and $w_1 = [w_1, w_2, w_3, w_4, w_5, w_6]^T$ is the ONS process noise vector.

3.2. *Measurement processing in the ONS.* Although different types of measurements can be used in autonomous navigation (Paluszek et al., 2010), the angles between a target (Mars, Phobos, or Deimos) and its background stars from images captured by navigation sensor is used as measurement (Figure 2), because this kind of measurement can avoid the attitude determination errors.

The image of the target and background stars is the original data from the navigation sensor (Camera). Several steps are required to obtain the angle between the target and the known stars:

Step 1: Centroid identification. The pixel and line of the target (p, l) and those of the optical axis (p_0, l_0) can be calculated from the image by centroid-identification image processing technology.

Step 2: Coordinate Transformations

(1) Coordinates transformation from the pixel coordinate frame to the 2-Dimension (2D) image coordinate frame.

The pixel and line coordinates (p, l) (Figure 3) can be described in the 2D image frame as (x_{2d}, y_{2d}) :

$$[x_{2d} \ y_{2d}]^T = \mathbf{K}^{-1} \left([p \ l]^T - [p_0 \ l_0]^T \right) \tag{4}$$

where \mathbf{K} is the transformation matrix.

(2) Coordinates transformation from the 2D image coordinate frame to the 3-Dimension (3D) sensor coordinate frame.

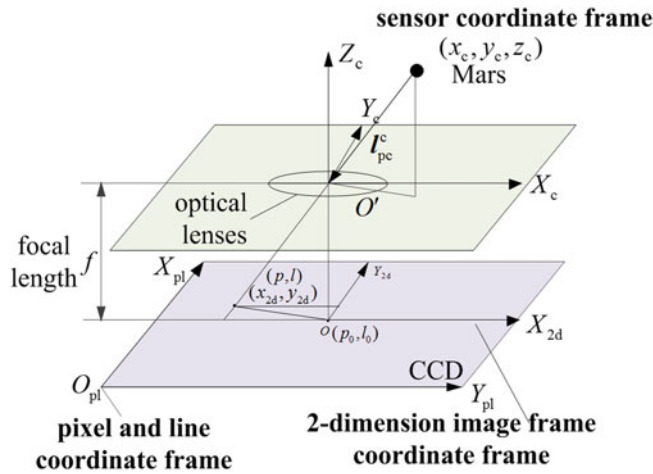


Figure 3. Coordinates definitions in navigation sensor.

A unit vector (x_c, y_c, z_c) in the 3D sensor coordinate frame can be given as follows:

$$l_{pc}^c = [x_c \ y_c \ z_c]^T = [x_{2d} \ y_{2d} \ -f]^T / \sqrt{x_{2d}^2 + y_{2d}^2 + f^2} \tag{5}$$

where, f is the focal length, and l_{pc}^c is the unit vector from the celestial body (c) to the probe (p) with respect to the origin in the sensor coordinate frame.

Step 3: Angle calculation. The angle θ between the target vector and its background star vector can be calculated by

$$\theta = \arccos \left[(-l_{pc}^c) \cdot (-l_s^c) \right] \tag{6}$$

where l_{pc}^c, l_s^c are the vectors from the target and the background star to the probe in the sensor coordinate frame derived from Step 2.

3.3. *The measurement model in the ONS.* The angles between Mars, Phobos and Deimos and their j th background star $\theta_{mj}, \theta_{pj}, \theta_{dj}$ can be expressed as

$$\begin{cases} \theta_{mj} = \arccos \left[(-l_{pm}^c) \cdot (-l_{1sj}^c) \right] = \arccos \left[(-l_{pm}^i) \cdot (-l_{1sj}^i) \right] \\ \theta_{pj} = \arccos \left[(-l_{pp}^i) \cdot (-l_{2sj}^i) \right] \\ \theta_{dj} = \arccos \left[(-l_{pd}^i) \cdot (-l_{3sj}^i) \right] \end{cases} \tag{7}$$

where in the sensor coordinate system, l_{pm}^c is the unit vector from Mars to the probe, l_{1sj}^c is the unit vector of the j th known star from the Mars image. In the TCI system, $l_{pm}^i, l_{pp}^i, l_{pd}^i$ are the unit vectors to the probe from Mars, Phobos, and Deimos respectively, $l_{1sj}^i, l_{2sj}^i, l_{3sj}^i$ are the unit vectors of the j th known star from the Mars image, Phobos image, and Deimos image, respectively.

Thus, the measurement model can be written in the general form:

$$Z_1(t) = h_1(X_1(t), t) + v_1(t) \tag{8}$$

where $\mathbf{Z}_1 = [\theta_{m1}, \theta_{m2}, \theta_{m3}, \theta_{p1}, \theta_{p2}, \theta_{p3}, \theta_{d1}, \theta_{d2}, \theta_{d3}]^T$ is the measurement vector, and $\mathbf{v}_1 = [v_{\theta_{m1}}, v_{\theta_{m2}}, v_{\theta_{m3}}, v_{\theta_{p1}}, v_{\theta_{p2}}, v_{\theta_{p3}}, v_{\theta_{d1}}, v_{\theta_{d2}}, v_{\theta_{d3}}]^T$ is the measurement noise vector, and $v_{\theta_{m1}}, v_{\theta_{m2}}, v_{\theta_{m3}}, v_{\theta_{p1}}, v_{\theta_{p2}}, v_{\theta_{p3}}, v_{\theta_{d1}}, v_{\theta_{d2}}, v_{\theta_{d3}}$ are the measurement noise.

3.4. *The initial state error of the ONS.* The initial state error of the ONS is the position and velocity error in the TCI system at the initial moment, which is delivered from the navigation results in the HCI system at the end of the cruise phase.

Consequently, the target ephemeris error could be reflected as a part of the initial navigation error in the approach phase. Therefore the initial navigation error $d\mathbf{X}_1(0)$ can be divided into two parts as follows:

$$d\mathbf{X}_1(0) = d\mathbf{X}^{\text{helio}}(0) + d\mathbf{X}_{\text{target}}^{\text{helio}}(0) \tag{9}$$

where $d\mathbf{X}^{\text{helio}}(0)$ is the initial navigation error with respect to the Sun, $d\mathbf{X}_{\text{target}}^{\text{helio}}(0)$ is the prior knowledge of the target ephemeris error at the initial moment.

4. RADIO NAVIGATION SUBSYSTEM (RNS)

4.1. *The force model in the RNS.* The RNS force model is established in the Helio-Centric Inertial (HCI) coordinate system:

$$\begin{cases} \dot{\mathbf{r}}' = \mathbf{v}' \\ \dot{\mathbf{v}}' = -\mu_s \frac{\mathbf{r}'}{r_{ps}^3} - \sum_i^N \mu_i \left[\frac{\mathbf{r}' - \mathbf{r}'_i}{r_{pi}^3} + \frac{\mathbf{r}'_i}{r_{si}^3} \right] + \mathbf{w}' \end{cases} \tag{10}$$

where in the HCI system, $\mathbf{r}' = [x', y', z']^T$ is the probe position vector, $\mathbf{v}' = [v'_x, v'_y, v'_z]^T$ is the probe velocity vector, $\mathbf{r}'_i = [x'_i, y'_i, z'_i]^T$ is the position vector of the i th planet, and $\mathbf{w}' = [w'_x, w'_y, w'_z]^T$ are the process noises in the three-axis velocity.

The force model can be written in the general form:

$$\dot{\mathbf{X}}_2(t) = f_2(\mathbf{X}_2(t), t) + \mathbf{w}_2(t) \tag{11}$$

where $\mathbf{X}_2 = [x', y', z', v'_x, v'_y, v'_z]^T$ is the RNS state vector, $f_2(\cdot)$ is the RNS dynamic model function, and $\mathbf{w}_2 = [w'_1, w'_2, w'_3, w'_4, w'_5, w'_6]^T$ is the RNS process noise vector.

4.2. *Measurements processing in the RNS.* Range and range rate are two available measurements of the RNS. The range rate between a probe and a station \dot{R} is measured by the signal frequency shift.

$$\dot{R} = c[1 - (f'_{\text{rec}} - \delta f_{\text{atm}} - \delta f_0) / f_0] \tag{12}$$

where c is the speed of light, f_0 is the frequency of the signal from the station, f'_{rec} is the frequency of the signal received by the station, $\delta f_{\text{atm}}, \delta f_0$ are the frequency errors caused by the atmospheric delay and the oscillator instability.

The range R between a probe and a station is measured by the signal delay time, and it can be expressed as

$$R = c\tau + c\delta t_R - c\delta t_T + \delta\rho_{\text{atm}} + \delta\rho_{\text{trop}} + \delta\rho_{\text{ion}} + \varepsilon \tag{13}$$

where τ is the signal transit time, δt_R is the receiver clock difference with true time, δt_T is the transmitter clock difference with true time, $\delta\rho_{\text{atm}}, \delta\rho_{\text{ion}}$ are the atmospheric delay contribution and ionosphere contribution, $\delta\rho_{\text{trop}}$ is the troposphere delay, and ε

represents remaining errors, such as the instrument noise (Vallado, 2007; Bar-Shalom et al., 2001).

4.3. *The measurement model in the RNS.* Ground stations can determine the probe position and velocity by measuring the ranges and range rates. A primary station with several secondary stations can accomplish the observing mission. The expressions of the range and range rate are given in the vector form by

$$\begin{cases} \boldsymbol{\rho} = (x' - x_f)\mathbf{u}_X + (y' - y_f)\mathbf{u}_Y + (z' - z_f)\mathbf{u}_Z \\ \dot{\boldsymbol{\rho}} = (v_x - v_{x_f})\mathbf{u}_X + (v_y - v_{y_f})\mathbf{u}_Y + (v_z - v_{z_f})\mathbf{u}_Z \end{cases} \quad (14)$$

where $\boldsymbol{\rho}$ is the probe position vector with respect to the ground station, $\dot{\boldsymbol{\rho}}$ is the relative probe velocity with respect to the ground station, $\rho, \dot{\rho}$ is the magnitude of $\boldsymbol{\rho}, \dot{\boldsymbol{\rho}}$, (x_f, y_f, z_f) are the coordinates of the ground station in the HCI system, and $\mathbf{u}_x, \mathbf{u}_y, \mathbf{u}_z$ are position unit vector of the probe with respect to the ground station.

Therefore, the measurement model can be written in the general form

$$\mathbf{Z}_2(t) = h_2(\mathbf{X}_2(t), t) + \mathbf{v}_2(t) \quad (15)$$

where $\mathbf{Z}_2 = [\rho_1, \dot{\rho}_1, \rho_2, \dot{\rho}_2, \rho_3, \dot{\rho}_3]^T$ is the measurement vector of the RNS, $\mathbf{v}_2 = [v_{\rho_1}, v_{\dot{\rho}_1}, v_{\rho_2}, v_{\dot{\rho}_2}, v_{\rho_3}, v_{\dot{\rho}_3}]^T$ is the measurement noise vector of the RNS, $\rho_1, \dot{\rho}_1, \rho_2, \dot{\rho}_2, \rho_3, \dot{\rho}_3$ are the range and the range rate between the probe and the 1st, 2nd, and 3rd ground stations, and $v_{\rho_1}, v_{\dot{\rho}_1}, v_{\rho_2}, v_{\dot{\rho}_2}, v_{\rho_3}, v_{\dot{\rho}_3}$ is the measurement noise.

4.4. *The initial state error of the RNS.* The navigation results at the end of the cruise phase and the initial state error are both in the HCI system. Therefore, the initial navigation error $d\mathbf{X}_2(0)$ is equal to the navigation results at the end of the cruise phase

$$d\mathbf{X}_2(0) = d\mathbf{X}^{\text{helio}}(0) \quad (16)$$

5. UNCERTAINTIES IN THE FORCE MODEL. To determine the main uncertainties in the force model and the process noise covariance, the uncertainties in the force model and their perturbation acceleration are analysed.

5.1. *Uncertainties of the gravity force of central body.* When the probe enters into the gravitational sphere of influence of the target, the target is the central body. The acceleration from the central body is

$$\mathbf{a}_{cb} = -\mu_t/\mathbf{r}^3 \quad (17)$$

where μ_t is the gravitational parameter of the target.

For a Mars probe in the approach phase ($R_m < r \leq 600000$ km, R_m is the radius of the Mars), the acceleration from the central body is $1.1897 \times 10^{-4} < a_{cb} \leq 3.4962$ m/s². Figure 4 gives the variation of the acceleration from the central body with the distance between the probe and Mars.

5.1.1. *Uncertainty of the target ephemeris.* The acceleration with respect to $\delta\mathbf{r}$, the changes in the target ephemeris, can be derived from the error propagation model of the target ephemeris (Ma et al., 2015)

$$\delta\dot{\mathbf{v}} = \mathbf{g}'(\mathbf{r})\delta\mathbf{r} \quad (18)$$

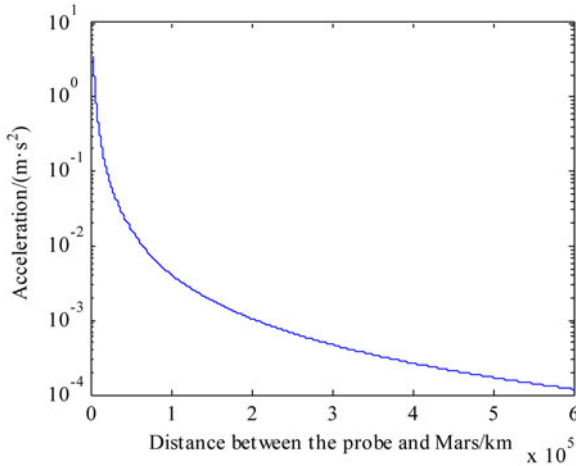


Figure 4. The central body gravitational acceleration of the Mars probe.

where $g(\mathbf{r}) = -\mu_t \mathbf{r}/r^3$, $\delta \dot{\mathbf{v}} = \delta \ddot{\mathbf{r}}$. It can be rewritten as follows:

$$\delta \ddot{\mathbf{r}} = -\mu_t \left[\frac{\delta \mathbf{r}}{r^3} - 3 \frac{\mathbf{r}(\mathbf{r} \cdot \delta \mathbf{r})}{r^5} \right] \tag{19}$$

where $\delta \ddot{\mathbf{r}}$ is the acceleration with respect to the target ephemeris uncertainty, $\delta \mathbf{r}$ is the target position error.

For a Mars probe in the approach phase, the ephemeris uncertainty of the central body (Mars) is less than 10 km, and the acceleration error caused by the Mars ephemeris uncertainty is about $O(10^{-4})$.

5.1.2. *Uncertainty of the target gravitational constant.* The derivative of acceleration with respect to $\delta \mu_t$, the change in the target gravitational parameter, can be derived from the error propagation model

$$\delta \ddot{\mathbf{r}} = (\mathbf{r}/r^3) \delta \mu_t \tag{20}$$

For a Mars probe in the approach phase, the gravitational parameter uncertainty of Mars is $\pm 0.1 \text{ km}^3/\text{s}^2$, and the perturbation acceleration error caused by the Mars gravitational parameter uncertainty is about $O(10^{-5} \sim 10^{-10})$, which can be reasonably ignored due to the small magnitude.

5.2. *Uncertainties of the perturbation of third body.* Besides the gravities of the central body, other planets, and Sun, gravities from other celestial bodies, such as natural satellites and asteroids also act on the probe. The perturbation acceleration model is

$$\mathbf{a}_N = -\mu_i \left[\frac{\mathbf{r}_{pi}}{r_{pi}^3} - \frac{\mathbf{r}_{ti}}{r_{ti}^3} \right] \tag{21}$$

where \mathbf{r}_{pi} is the position vector from the third body to the probe, and \mathbf{r}_{ti} is the position vector from the third body to the target.

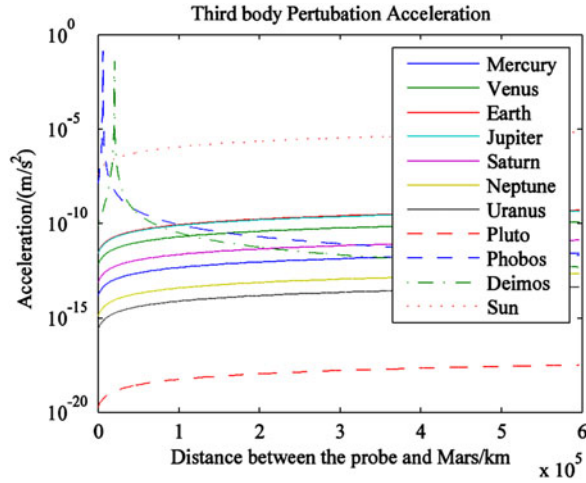


Figure 5. Third body gravitational perturbation acceleration.

For a Mars probe in the approach phase, $r \ll (r_{ti}, r_{pi})$ and $r_{pi}^3 \approx r_{ti}^3$, then the perturbation acceleration model can be simplified as follows

$$a_N = -\mu_i r / r_{pi}^3 (\mathbf{r}/r) \tag{22}$$

Figure 5 gives the third body perturbation acceleration of all planets except Mars for a Mars probe in the approach phase, which indicates that the main third body perturbation acceleration is from the Sun, and the perturbation acceleration from the other bodies is less than 10^{-10} m/s^2 . The third body perturbation acceleration from Phobos and Deimos is $10^{-1} \sim 10^{-5} \text{ m/s}^2$ at a low altitude, which cannot be ignored.

5.3. *Uncertainties of the gravity field of the target.* As the target is not a perfectly spherical central body, the perturbing accelerations caused by a non-spherical central body will affect the force model accuracy. Taking Mars as an example, the aspherical-potential function U is modelled in spherical harmonics using the expression (Vallado, 2007; Lemonine et al., 2001)

$$U = \frac{\mu_t}{r} \sum_{n=2}^{N_{\max}} \left(\frac{R_m}{r} \right)^n \sum_{m=0}^n (C_{nm} \cos m\lambda + S_{nm} \sin m\lambda) P_{nm}(\cos \phi) \tag{23}$$

where, r, θ, λ are the body fixed coordinates, ϕ is latitude, and λ is longitude, C_{nm} and S_{nm} are the normalised coefficients of the spherical harmonic expansion, and P_{nm} are the normalised associated Legendre Functions.

Different Mars gravity field models are established by experimental data from interplanetary missions, such as GMM-2B, MGS75D, MGS95J, MRO110B, etc. The degree and order of the model determines the accuracy of the model. GMM-2B is an 80×80 spherical harmonics model calculated by Goddard Space Flight Center (GSFC), and MGS75D, MGS95J, MRO110B are $75 \times 75, 95 \times 95, 110 \times 110$ spherical harmonics models calculated by the Jet Propulsion Laboratory (JPL). Normalised gravitational coefficients of GMM-2B can be found in Lemonine (2001).

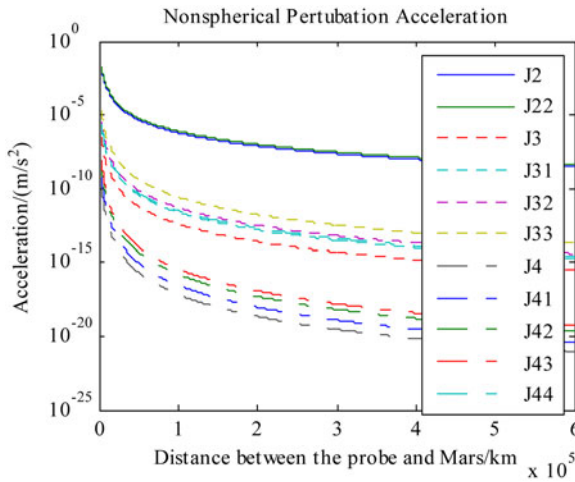


Figure 6. Mars 4×4 nonspherical perturbation acceleration.

Figure 6 gives the 4×4 nonspherical perturbation acceleration for a Mars probe in the approach phase. For a Mars probe in the approach phase, $J_2 \approx O(10^{-4})$, $J_{2,2} \approx O(10^{-4})$, $J_{3,m} \approx O(10^{-10}) \sim O(10^{-6})$ and $J_{4,m} \approx O(10^{-18}) \sim O(10^{-9})$.

5.4. *Uncertainties of Solar radiation perturbation.* When the probe is traveling in space, it is exposed to the Sun. Some incoming radiation from the Sun is absorbed, while some is reflected. The energy conversion leads to a force on the probe, which is the solar radiation pressure. Then the acceleration caused by solar radiation pressure can be modelled as

$$\mathbf{a}_s = -c_R p_{SR} (A/m) \mathbf{r}_{\text{sat}\odot} / |\mathbf{r}_{\text{sat}\odot}| \tag{24}$$

where c_R is the reflectivity, its value depends on the composition and shape of the probe. If all the radiation is absorbed or reflected, then $c_R = 1$ or $c_R = 2$. If the object is translucent to incoming radiation, then $c_R = 0$. A is the incident area exposed to the Sun. p_{SR} is the force of solar pressure per unit area, and $\mathbf{r}_{\text{sat}\odot}$ is the position vector from the probe to the Sun.

If the ratio of incident area to mass $A/m = 0.02 \text{ m}^2/\text{kg}$, and the average radiated power of solar radiation per unit area is 1.4 W/m^2 , then the solar radiation pressure is $p_{SR} = 4.65 \times 10^{-6} \text{ N/m}^2$. For a Mars probe in the approach phase, the solar radiation perturbation acceleration is less than 10^{-7} m/s^2 .

5.5. *Uncertainties of atmosphere perturbation.* Mars, Venus, Neptune and Titan are all surrounded by atmosphere. If the probe is operated at high speed in the atmosphere, the atmospheric drag will decrease the orbit altitude. The basic model is

$$\mathbf{a}_D = -C_D A_D \rho v^2 / 2m (\mathbf{v}/v) \tag{25}$$

where C_D is the coefficient of drag, A_D is the exposed cross-sectional area, ρ is the atmospheric density, and \mathbf{v} is the velocity of the probe relative to the atmosphere.

For Mars exploration, the available Mars atmosphere models include Mars GRAM 2010, Mars GRAM 2005, Mars GRAM 2000, etc. The atmospheric density depends

on the altitude of the orbit. The atmospheric density and its drag effects decrease as the altitude rises. The atmospheric densities at 100 km and 50 km above the Mars surface are $7.5 \times 10^{-9} \text{ kg/m}^3$ and $5.6 \times 10^{-11} \text{ kg/m}^3$, respectively.

If the altitude $h = 150 \text{ km}$, the density is $\rho = 5.6 \times 10^{-11} \text{ kg/m}^3$, the coefficient of drag C_D is approximately 1, and the ratio of incident area to mass $A_D/m = 0.02 \text{ m}^2/\text{kg}$, then for a Mars probe in the approach phase, $a_D < 1 \times 10^{-5} \text{ m/s}^2$.

5.6. *Total uncertainties of the force model.* According to the analysis above, for a Mars probe in the approach phase, the uncertainties in the force models can be determined. The two main kinds of perturbation acceleration come from the gravity field of the target and target ephemeris uncertainty, and it is about 10^{-4} m/s^2 . The other perturbation acceleration caused by solar radiation pressure, atmosphere drag and the target gravitational parameter can be reasonably ignored due to their small magnitude.

6. FILTER METHODS, EPHEMERIS CORRECTION AND INFORMATION FUSION

6.1. *Filter methods for two navigation subsystems.* Because of the nonlinear problem of the force models, a nonlinear filter should be used. Extended Kalman Filter (EKF) (Lee and Kyle, 2004), Unscented Kalman Filter (UKF) (Julier and Uhlmann, 1997; Julier et al., 2000), and Unscented Particle Filter (UPF) (van der Merwe et al., 2000; Payne and Marrs, 2004) are three well-known nonlinear filters. EKF is based on the analytical Taylor series expansion of the nonlinear state and measurement models and the state approximations introduce large errors due to the neglected nonlinearities. UKF is a method capturing the mean and covariance of the state using the true nonlinear models and a set of sigma sample points with the unscented transformation. These two methods have the limitation that they do not apply to a general non-Gaussian distribution. The Particle Filter (PF) implements a recursive Bayesian filter by Monte Carlo simulations. The performance of the PF heavily depends on the choices of the importance sampling density and resampling scheme, and the number of samples decides the time consumed. However, due to the strict real time and accuracy requirement, the time consuming characteristics of PF and the inaccuracy of EKF, UKF is used in the INS (Ning et al., 2012b).

6.2. *Target ephemeris correction.*

6.2.1. *The analytical method for target ephemeris correction.* The target ephemeris uncertainty can be calculated from the geometry of the Sun, Earth, the actual target, the target in ephemeris and the probe (Figure 7).

From Figure 7, the target ephemeris uncertainty Z_{err} can be derived from

$$Z_{\text{err}} = X_{\text{target}}^{\text{a}} - X_{\text{target}}^{\text{p}} \quad (26)$$

where, $X_{\text{target}}^{\text{p}}$ and $X_{\text{target}}^{\text{a}}$ are the predicted and actual target position vector in the HCI system, $X_{\text{target}}^{\text{p}}$ can be obtained from target ephemeris database, and $X_{\text{target}}^{\text{a}}$ can be calculated by

$$X_{\text{target}}^{\text{a}} = X_{\text{target}}^{\text{helio}} \quad (27)$$

where $X_{\text{target}}^{\text{helio}}$ can be measured from the results of the RNS and the ONS, as Equation (1) shows. Therefore, the target ephemeris uncertainty Z_{err} can be

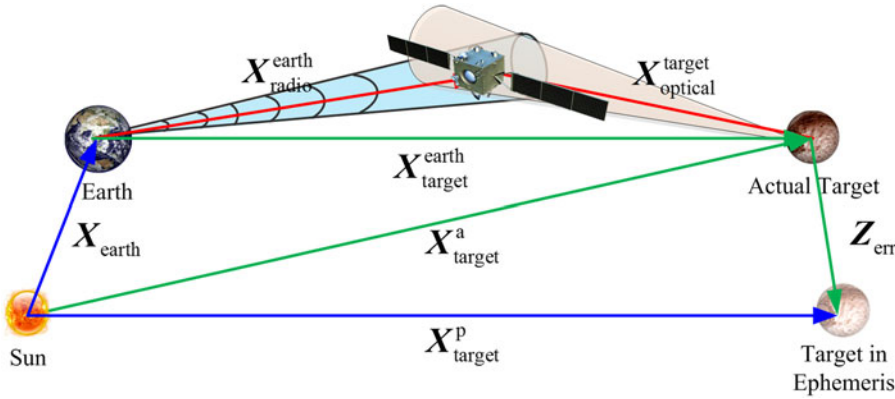


Figure 7. Geometry of the Sun, Earth, the Actual Target, the Target in ephemeris and the Interplanetary probe.

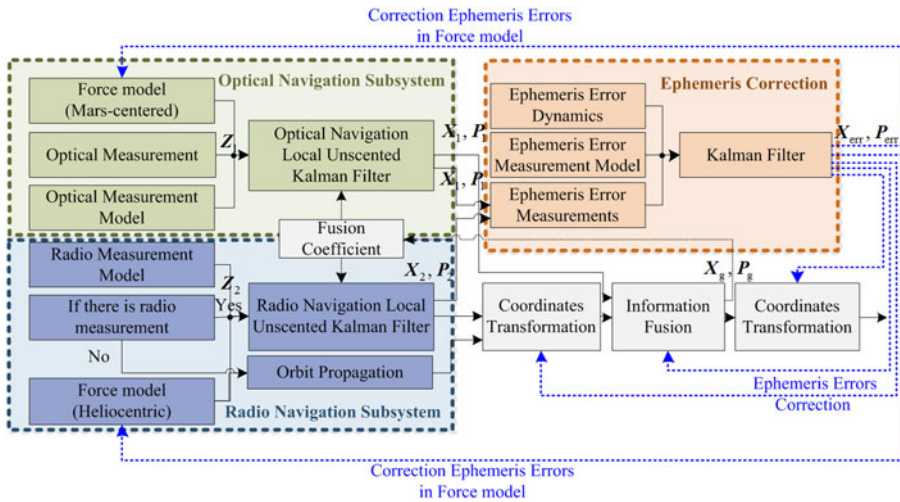


Figure 8. Navigation system flow chart.

calculated as follows:

$$Z_{err} = X_{radio}^{helio} - X_{optical}^{target} - X_{target}^p \tag{28}$$

6.2.2. *The estimation method for target ephemeris correction.* The ephemeris uncertainty leads to a high uncertainty of the probe position. The exact orientation of orbit plane is more uncertain, whereas the period of the planet motion is relatively accurate. Thus the magnitude of the velocity typically has accurate prior knowledge. Based on those facts, the target ephemeris error is modelled as constant (Ma et al., 2015; Wang et al, 2013).

Figure 8 shows the flow chart of the target ephemeris correction, and the specific steps are given as follows:

(1) *The state model of target ephemeris error.* Since the variation of the target ephemeris error is slow in each filter period, the dynamics of the target ephemeris error can be modelled as:

$$\dot{\mathbf{X}}_{\text{err}} = 0 \quad (29)$$

where $\dot{\mathbf{X}}_{\text{err}} = [\dot{x}_{\text{err}} \ \dot{y}_{\text{err}} \ \dot{z}_{\text{err}}]^T$, $(x_{\text{err}}, y_{\text{err}}, z_{\text{err}})$ are the coordinates of the target ephemeris errors in the HCI system.

The discrete state model of the target ephemeris error can be given as

$$\mathbf{X}_{\text{err}}(k+1) = F_{\text{err}}(\mathbf{X}_{\text{err}}(k), k) + \mathbf{w}_{\text{err}}(k) \quad (30)$$

where the mapping $F_{\text{err}}(\cdot)$ represents the process models and $F_{\text{err}}(\mathbf{X}_{\text{err}}(k), k) = \Phi_{\text{err},k+1,k} \mathbf{X}_{\text{err},k}$, $\Phi_{\text{err},k+1,k}$ is the state transition matrix at step k , $\mathbf{X}_{\text{err}}(k)$ is the state vector at step k and $\mathbf{w}_{\text{err}}(k)$ is the process noise vector.

(2) *Measurement and its model.* The measurement vector of the target ephemeris error \mathbf{Z}_{err} can be obtained from the estimation of the ONS and the RNS, $\mathbf{X}_{\text{optical}}^{\text{target}}$ and $\mathbf{X}_{\text{radio}}^{\text{helio}}$

$$\mathbf{Z}_{\text{err}} = \mathbf{X}_{\text{radio}}^{\text{helio}} - \mathbf{X}_{\text{optical}}^{\text{target}} - \tilde{\mathbf{X}}_{\text{target}}^e \quad (31)$$

where $\tilde{\mathbf{X}}_{\text{target}}^e$ is the estimation of target ephemeris vector.

Accordingly, the discrete measurement model of the target ephemeris error can be expressed as follows:

$$\mathbf{Z}_{\text{err}}(k) = h_3(\mathbf{X}_{\text{err}}, k) + \mathbf{v}_3(k) \quad (32)$$

where $\mathbf{Z}_{\text{err}}(k)$ is the measurement vector of ephemeris error at step k , the mapping $h_3(\cdot)$ represents the measurement models function, and $\mathbf{v}_3(k)$ is the measurement noise vector of ephemeris errors at the step k .

(3) *KF.* According to the linear characteristics of the state model and measurement models of the ephemeris error, KF is utilised to estimate the target ephemeris error $\hat{\mathbf{X}}_{\text{err},k}$ and its covariance matrix $\mathbf{P}_{\text{err},k}$.

(4) *Correction.* $\hat{\mathbf{X}}_{\text{err},k}$ and $\mathbf{P}_{\text{err},k}$ are provided for the force models of both RNS and ONS to correct the target ephemeris error. After the correction, the accuracy of the orbit dynamics is enhanced.

1) *Correction on the force model of the ONS.* In the ONS, the coordinates of all the celestial bodies are in the TCI system. Therefore, the target ephemeris error has no effect on the coordinates of the origin of the TCI system, and the coordinates of the actual target are $[0, 0, 0]^T$. However, the coordinates of other planets contain the Mars ephemeris errors owing to the coordinates transformation.

The i th celestial body position coordinates in the TCI system $\mathbf{X}_i^{\text{target}}$ can be expressed as

$$\mathbf{X}_i^{\text{target}} = \mathbf{X}_i^{\text{helio}} - \mathbf{X}_{\text{target}}^{\text{helio}} - \mathbf{X}_{\text{err}} \quad (33)$$

where $\mathbf{X}_i^{\text{helio}}$ is the position coordinates of the i th celestial body in the HCI system, $\mathbf{X}_{\text{target}}^{\text{helio}}$ is the actual target ephemeris in the HCI system, \mathbf{X}_{err} is the target ephemeris error, and $\tilde{\mathbf{X}}_{\text{target}}^{\text{helio}} = \mathbf{X}_{\text{target}}^{\text{helio}} + \mathbf{X}_{\text{err}}$. Therefore, the ephemerides of other planets (or the Sun) used in the force model are affected by the target ephemeris error \mathbf{X}_{err} , and the

estimated target ephemeris error is used to correct the ephemerides of other planets in the state model

$$\mathbf{X}_i^{\text{target}} = \mathbf{X}_i^{\text{helio}} - \mathbf{X}_{\text{target}}^{\text{helio}} - \mathbf{X}_{\text{err}} + \hat{\mathbf{X}}_{\text{err}} = \mathbf{X}_i^{\text{helio}} - \tilde{\mathbf{X}}_{\text{target}}^{\text{helio}} + \hat{\mathbf{X}}_{\text{err}} \tag{34}$$

where, $\hat{\mathbf{X}}_{\text{err}}$ is the estimated target ephemeris error.

2) *Correction of the force model of the RNS.* In the RNS, the coordinates of all the celestial bodies are in the HCI system. The target ephemeris error only affects the coordinates of the target, and the corrected target ephemeris is given by

$$\hat{\mathbf{X}}_{\text{target}}^{\text{helio}} = \mathbf{X}_{\text{target}} - \mathbf{X}_{\text{err}} + \hat{\mathbf{X}}_{\text{err}} = \tilde{\mathbf{X}}_{\text{target}}^{\text{helio}} + \hat{\mathbf{X}}_{\text{err}} \tag{35}$$

where $\hat{\mathbf{X}}_{\text{target}}^{\text{helio}}$ is the corrected target ephemeris.

6.3. *Information fusion algorithm.* $\mathbf{X}_1(k)$, $\mathbf{P}_1(k)$ and $\mathbf{X}_2(k)$, $\mathbf{P}_2(k)$ are the estimated values and error covariance matrix of ONS and RNS respectively. However, $\mathbf{X}_1(k)$, $\mathbf{P}_1(k)$ are described in the TCI system, whereas $\mathbf{X}_2(k)$, $\mathbf{P}_2(k)$ are in the HCI system. To integrate the information in the same coordinate system, $\mathbf{X}_2(k)$, $\mathbf{P}_2(k)$ are transformed to $\mathbf{X}'_2(k)$, $\mathbf{P}'_2(k)$ in the TCI system (see 6.4. *Coordinates Transformation*). The global optimal estimation and its error covariance \mathbf{X}_g and \mathbf{P}_g in the TCI system in the master filter is obtained by the following equations (Ning and Fang, 2008):

$$\mathbf{X}_g(k) = \mathbf{P}_g(k) [\mathbf{P}_1^{-1}(k)\mathbf{X}_1(k) + \mathbf{P}'_2^{-1}(k)\mathbf{X}'_2(k)] \tag{36}$$

$$\mathbf{P}_g(k) = [\mathbf{P}_1^{-1}(k) + \mathbf{P}'_2^{-1}(k)]^{-1} \tag{37}$$

$$\hat{\mathbf{X}}_i(k) = \mathbf{X}_g(k) \tag{38}$$

$$\mathbf{P}_i(k) = \beta_i \cdot \mathbf{P}_g^{-1}(k) \tag{39}$$

$$\beta_1 + \beta_2 = 1 \tag{40}$$

where β_i is the fusion coefficient, which is inversely proportional to the trace of the error covariance.

The stability of UKF is not as good as EKF, so the feedback is only performed to state variables of the position and velocity. The information fusion algorithm directly provides the navigation results with respect to Mars. Those with respect to Earth can be derived by coordinate transformation using updated ephemeris.

6.4. *Coordinates Transformations*

6.4.1. *Coordinates Transformation from the HCI to TCI system.* To integrate the information in the same system, the navigation results of the RNS $\mathbf{X}_2(k)$, $\mathbf{P}_2(k)$ in the HCI system are transformed to $\mathbf{X}'_2(k)$, $\mathbf{P}'_2(k)$ in the TCI system. The translation between the two systems is

$$\mathbf{X}'_2 = \mathbf{X}_2 + \mathbf{X}_{\text{target}}^{\text{helio}} + \delta\mathbf{X}_{\text{target}}^{\text{helio}} \tag{41}$$

and

$$\mathbf{P}'_2 = \mathbf{P}_2 + \mathbf{P}_{\text{target}}^{\text{helio}} \tag{42}$$

where $\delta\mathbf{X}_{\text{target}}^{\text{helio}}$ is the ephemeris error of $\mathbf{X}_{\text{target}}^{\text{helio}}$, $\mathbf{P}_{\text{target}}^{\text{helio}}$ is the target ephemeris covariance, $\mathbf{P}_{\text{target}}^{\text{helio}} = \mathbf{P}_{\text{err}}$.

6.4.2. *Coordinates Transformation from the TCI system to ECI.* To simultaneously provide the position and velocity with respect to Earth and the target, the results of the INS in the TCI system need to transform these in the ECI system, which can be expressed as follows

$$\mathbf{X}'_g = \mathbf{X}_g - \mathbf{X}_{\text{target}}^{\text{helio}} - \delta\mathbf{X}_{\text{target}}^{\text{helio}} + \mathbf{X}_{\text{earth}}^{\text{helio}} + \delta\mathbf{X}_{\text{earth}}^{\text{helio}} \quad (43)$$

and

$$\mathbf{P}'_g = \mathbf{P}_g + \mathbf{P}_{\text{target}}^{\text{helio}} \quad (44)$$

where, \mathbf{X}'_g and \mathbf{P}'_g is the estimation and its covariance of the INS in the ECI system, $\delta\mathbf{X}_{\text{earth}}^{\text{helio}}$ is the ephemeris error of $\mathbf{X}_{\text{earth}}^{\text{helio}}$ which can be neglected owing to the long-term observation of the Sun from Earth.

6.5. *Criterion of final navigation results.*

6.5.1. *Final navigation results with respect to the target.* Besides the INS, ONS alone can also provide the navigation result with respect to the target. The final navigation estimation $\mathbf{X}_g^{\text{target}}$ and its covariance $\mathbf{P}_g^{\text{target}}$ with respect to the target is chosen by their covariance as follows:

$$\begin{cases} \mathbf{P}_g^{\text{target}} = \mathbf{P}_g, \mathbf{X}_g^{\text{target}} = \mathbf{X}_g & \text{if } \mathbf{P}_g < \mathbf{P}_1 \\ \mathbf{P}_g^{\text{target}} = \mathbf{P}_1, \mathbf{X}_g^{\text{target}} = \mathbf{X}_1 & \text{if } \mathbf{P}_1 < \mathbf{P}_g \end{cases} \quad (45)$$

6.5.2. *Final navigation results with respect to Earth.* Similarly, RNS alone can also provide the navigation result with respect to Earth. The final navigation estimation $\mathbf{X}_g^{\text{earth}}$ and its covariance $\mathbf{P}_g^{\text{earth}}$ with respect to Earth is chosen by their covariance as follows:

$$\begin{cases} \mathbf{P}_g^{\text{earth}} = \mathbf{P}'_g, \mathbf{X}_g^{\text{earth}} = \mathbf{X}'_g & \text{if } \mathbf{P}'_g < \mathbf{P}_2 \\ \mathbf{P}_g^{\text{earth}} = \mathbf{P}_2, \mathbf{X}_g^{\text{earth}} = \mathbf{X}_2 & \text{if } \mathbf{P}_2 < \mathbf{P}'_g \end{cases} \quad (46)$$

7. SIMULATIONS

7.1. *Simulation setup.* The satellite Tool Kit Astrogator was used for creating the trajectory of the probe Earth-Mars transfers in 2013. The initial parameters were set as shown in Table 2.

In the reference orbit model, the perturbation force included third body gravity from the Sun and other planets, spherical harmonic gravity of central body and solar radiation force. The spherical harmonic gravity of Mars was modelled as GMM2B (4×4) (Lemoine et al., 2001). Besides the gravitational perturbation from celestial bodies, solar radiation pressure was also included with the spherical solar radiation pressure model (Vallado, 2007). The reference orbit was generated by RKF89 numerical integrator using the fixed step (1 s).

The ephemerides of planetary bodies, the natural satellite and the star used JPL DE421 (Folkner, 2010), SPICE ephemeris (Acton, 1996), and Tycho-2 star catalogue, respectively (Høg et al., 2000). The optical characteristics of Mars, Phobos, and Deimos sensors are shown in Table 3. Three deep space stations were located in Kashi, Qingdao and Santiago. The available arcs are given in Figure 9.

Table 2. The initial parameters.

Parameters	Value
Launch Date	Nov. 13 2013
Arrival Date	Sept. 10 2014
C3	13.0753 km ² /s ²
RA	190.4091°
Dec	17.3471°
Simulation Period	20 Aug. 2014 ~ 1 Sep. 2014
Close Approach Time	10 Sep 2014 00:00:00-000
Perigee Altitude	264 km
A priori uncertainty wrt Mars	[1010 km, 1010 km, 1010 km, 1 m/s, 1 m/s, 1 m/s] ^T
Uncertainty Requirement wrt Mars	20 km
The accuracy level of optical sensor	0.1 pixel
The accuracy level of range	15 m
The accuracy level of range rate	1 mm/s
The target ephemeris uncertainty	[10000 m, 10000 m, 10000 m] ^T

Table 3. Characteristics of the sensors.

Characteristics	Value
Focal length, mm	2013.4
Field of view, mrad	10 × 10
Resolution, μrad/pixel	10
CCD format, pixels	1024 × 1024
Pixel size, μm	21

7.2. *Navigation results.* Firstly, the results of the RNS and the ONS are given. Secondly, the impacts of the ephemeris uncertainty on information fusion are provided. Finally, the information fusion results using the analytical method and the estimation method for ephemeris correction are also given to show the importance of ephemeris correction and superior performance of the proposed method.

7.2.1. *Navigation results of two navigation subsystems.* Figure 10 and Table 4 give the navigation results (both with respect to Earth and Mars) of the RNS and ONS. As shown in Figure 10 and Table 4, the RNS can provide accurate navigation performance with respect to Earth, and the estimation accuracy of the position is 1.4993 m and that of the velocity is 7.9599×10^{-6} m/s, which is because RNS directly measures the observations with respect to Earth rather than Mars. However, for RNS alone, because of the inaccurate Mars ephemeris, the estimated position error with respect to Mars is inferior to that with respect to Earth. Therefore, the RNS usually offers navigation results with respect to Earth in interplanetary missions.

Different from the RNS, the ONS provide accurate navigation performance with respect to Mars, that is 8.6747×10^3 m in position and 0.0356 m/s. That is because ONS directly measures the observations with respect to Mars rather than Earth, and its navigation performance with respect to Mars does not depend on the Mars ephemeris, but on the accuracy of the measurements and models. When the Mars ephemeris uncertainty changes, the accuracy with respect to Mars provided by the ONS remains the same. However, also because of the inaccurate Mars ephemeris,

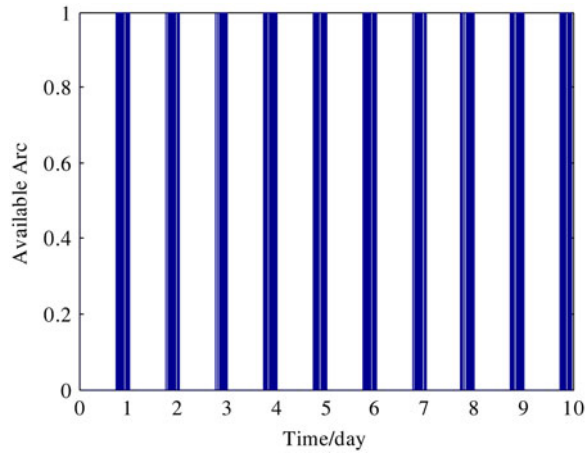


Figure 9. Available arcs of DSN station.

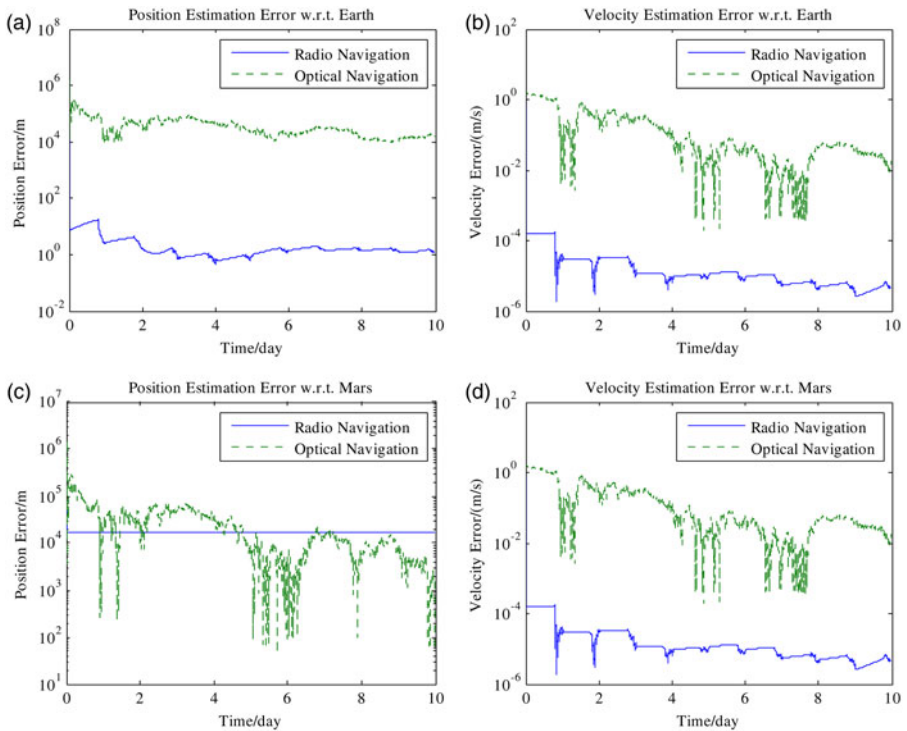


Figure 10. Performance comparisons of two navigation subsystems. (a) Position error (wrt Earth), (b) Velocity error (wrt Earth), (c) Position error (wrt Mars), (d) Velocity error (wrt Earth).

the ONS cannot provide accurate navigation results with respect to Earth. Therefore, the ONS usually provides navigation results with respect to the target in interplanetary missions.

Table 4. Navigation results of two navigation subsystems.

Method	Estimated Position Error(m)		Estimated Velocity Error(m/s)	
	wrt Earth	wrt Mars	wrt Earth	wrt Mars
Radio Only	1.4993	1.7322×10^4	7.9599×10^{-6}	7.9599×10^{-6}
Optical Only	2.0316×10^4	8.6747×10^3	0.0356	0.0356

Table 5. Results of information fusion with ephemeris uncertainty.

Method	Estimated Position Error(m)		Estimated Velocity Error(m/s)	
	wrt Earth	wrt Mars	wrt Earth	wrt Mars
without ephemeris uncertainty	1.3345	1.3345	0.0075	0.0075
ephemeris uncertainty	1.1818×10^4	8.2224×10^3	0.0217	0.0217
ephemeris uncertainty and criteria	1.4963	7.8062×10^3	7.8873×10^{-6}	0.0034

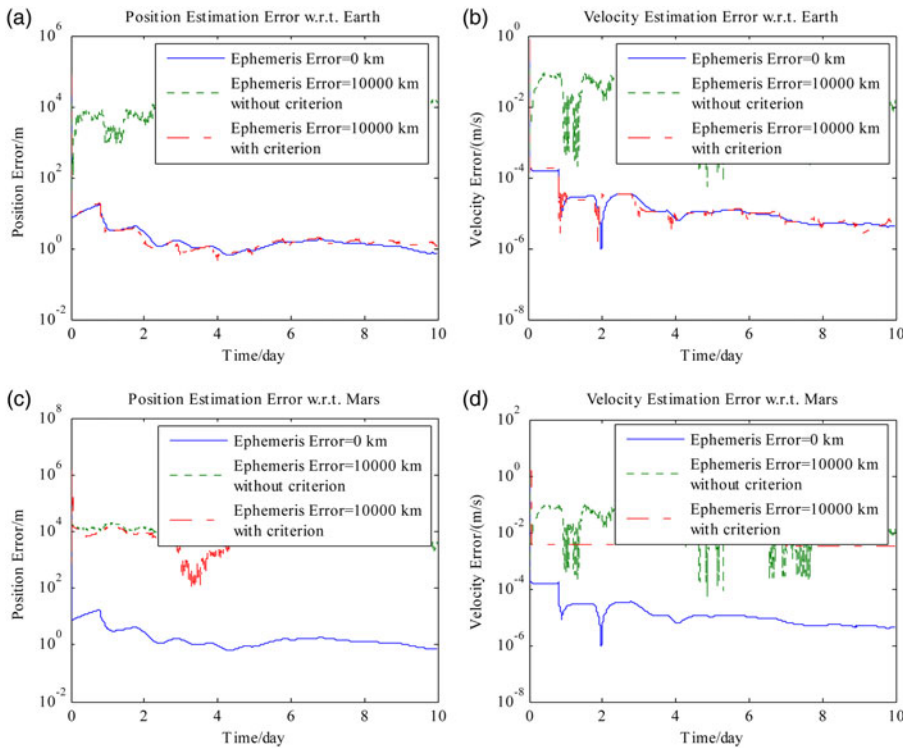


Figure 11. Impacts of ephemeris error on information fusion results. (a) Position error (wrt Earth), (b) Velocity error (wrt Earth), (c) Position error (wrt Mars), (d) Velocity error (wrt Mars).

7.2.2. *Fusion results with ephemeris uncertainty.* Both the fusion results with and without ephemeris uncertainty and the fusion results with and without criteria are shown in Figure 11 and Table 5. It can be seen that the fusion accuracy is heavily

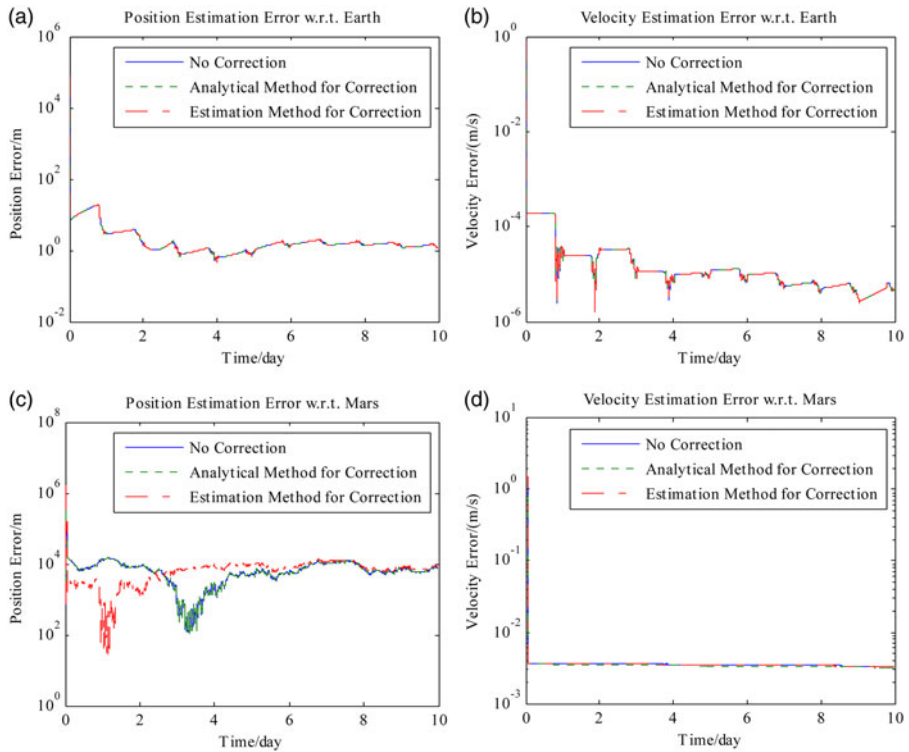


Figure 12. Information fusion results using estimation for ephemeris correction. (a) Position error (wrt Earth), (b) Velocity error (wrt Earth), (c) Position error (wrt Mars), (d) Velocity error (wrt Mars).

influenced by the Mars ephemeris uncertainty. Because the Mars ephemeris uncertainty polluted the estimated position with respect to Mars in the RNS, the direct fusion results without criteria with respect to Earth are worse than the RNS.

After using the criteria, compared with the subsystems alone, better accuracies with respect to Earth and Mars are achieved. This is because the criteria of final results integrate the more accurate results from each subsystem. However, compared with the result without ephemeris uncertainty, the accuracy has declined. Therefore, the Mars ephemeris uncertainty is still propagated into the INS, and its effects cannot be ignored.

7.2.3. Fusion results with ephemeris correction. Figure 12 and Table 6 compare the fusion results using three ephemeris correction methods, including no correction, the analytical method and the estimation method. The errors of the calculated and estimated ephemeris uncertainties from the analytical and estimation methods are given in Figure 13.

By using the analytical method, the estimation errors with respect to both Earth and Mars decline a little. After the Mars ephemeris is calculated and corrected, the accuracy with respect to Mars is improved and is better than the ONS results. The calculated error of the Mars ephemeris uncertainty is within 7·8075 km (shown in Figure 13). Therefore, although the improvement is not evident, the improvement is attributed

Table 6. Performance comparison of information fusion using different methods for ephemeris correction.

Method	Position Error (m)		Velocity Error(m/s)		Ephemeris Error/m
	wrt Earth	wrt Mars	wrt Earth	wrt Mars	
No correction	1.4963	7.8062×10^3	7.8873×10^{-6}	0.0034	–
Analytical method	1.4962	7.8061×10^3	7.8870×10^{-6}	0.0034	7.8075×10^3
Estimation	1.4961	4.4704×10^3	7.8867×10^{-6}	0.0034	4.4707×10^3

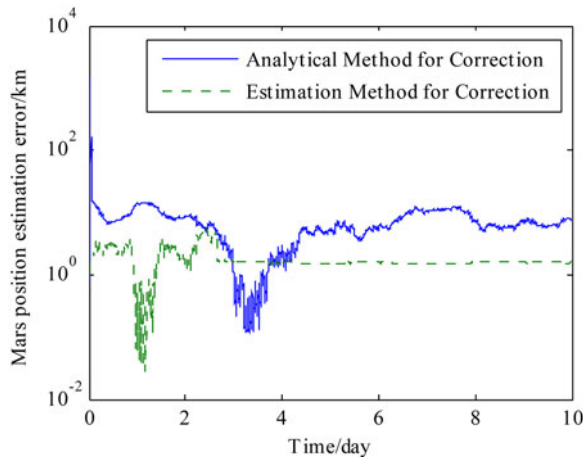


Figure 13. Estimation errors of ephemeris uncertainty.

to the analytical method for the ephemeris correction, which provides the INS with a better ephemeris uncertainty result.

By using the estimation method, the INS can achieve the best accuracy. In particular, the estimation errors of the position with respect to Mars decline from 7.8062 km to 4.4704 km . The estimation error of the Mars ephemeris uncertainty is within 4.4707 km (Figure 13). The accuracy with respect to both Earth and Mars improved because of the corrected force models. It is indicated that the improvement of the Mars ephemeris uncertainty is attributable to the Mars ephemeris uncertainty model and KF helping to reduce the measurement noise from the analytical solution.

Therefore, the utilisation of the estimation method to correct ephemeris leads to the accuracy enhancement, which precisely estimates the ephemeris uncertainty, corrects the errors in the force models and reduces the effects of the Mars ephemeris uncertainty on the estimation accuracy. These results suggest that information fusion using estimation for ephemeris correction is an attractive solution for the ephemeris uncertainty problem.

7.3. Impact factors of estimation accuracy. The estimation accuracy of the ephemeris error is influenced by the parameters in the KF, such as the initial ephemeris error and covariance, the process noise covariance and the measurement noise covariance. The following are the specific effects of the impact factors on the estimation accuracy.

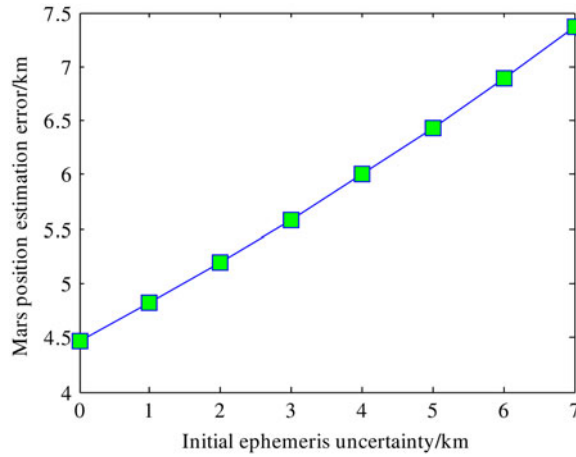


Figure 14. Impacts of initial errors on the estimation error of the ephemeris uncertainty.

7.3.1. *Initial ephemeris error and covariance.* The initial ephemeris error $\mathbf{X}_{\text{err}}(0)$ is the prior knowledge of the ephemeris uncertainty at the initial moment, and the initial ephemeris covariance is $\mathbf{P}_{\text{err}}(0) = \mathbf{E}(\mathbf{X}_{\text{err}}(0)\mathbf{X}_{\text{err}}(0)^T)$. The initial ephemeris error and covariance have some effects on the final estimation. Figure 14 and Table 7 give the estimation errors of the ephemeris uncertainty with different initial errors. From Figure 14 and Table 7, the estimation errors of ephemeris uncertainty increase with the initial ephemeris error growth.

7.3.2. *Process noise covariance.* The process noise covariance of the ephemeris uncertainty is defined as $\mathbf{Q}_{\text{err}} = \mathbf{E}[(\mathbf{W}_{\text{err}})(\mathbf{W}_{\text{err}})^T]$. However, the process noise covariance is presumed to be

$$\mathbf{Q}_{\text{err}} = q_0 \cdot \text{diag}[1, 1, 1]$$

Figure 15 and Table 8 give the estimation errors of the ephemeris uncertainty with different process noise covariance matrices, and q_0 varies from 10^{-5} to 10^{12} . From Figure 15 and Table 8, the estimation has the highest precision when $q_0 = 10^2$. It is suggested that only if the \mathbf{Q}_{err} matches the real process noise covariance, the estimation error is minimum. Therefore, the prior knowledge of the process noise covariance is required.

7.3.3. *Measurement noise covariance.* The measurement noise covariance of the ephemeris uncertainty is defined as $\mathbf{R}_{\text{err}} = \mathbf{E}[(\mathbf{V}_{\text{err}})(\mathbf{V}_{\text{err}})^T]$. In our case, the ideal one is equal to $\tilde{\mathbf{R}}_{\text{err}} = \mathbf{E}[(\mathbf{Z}_{\text{err}} - \tilde{\mathbf{X}}_{\text{err}})(\mathbf{Z}_{\text{err}} - \tilde{\mathbf{X}}_{\text{err}})^T]$, $\tilde{\mathbf{X}}_{\text{err}}$ is the real Mars ephemeris uncertainty. However, $\tilde{\mathbf{X}}_{\text{err}}$ is not exactly known in practice. Because Mars ephemeris uncertainty is approximately constant, the estimation at the last step $\mathbf{X}_{\text{err}}(k-1)$ can replace $\tilde{\mathbf{X}}_{\text{err}}$. Therefore $\mathbf{R}_{\text{err}}(k) = \mathbf{E}[(\mathbf{Z}_{\text{err}}(k) - \mathbf{X}_{\text{err}}(k-1))(\mathbf{Z}_{\text{err}}(k) - \mathbf{X}_{\text{err}}(k-1))^T]$ is used in simulations.

Figure 16 and Table 9 give the estimation errors of ephemeris uncertainty with different measurement noise covariance metrics. It is shown that the estimation is

Table 7. Estimation accuracy with different initial errors.

Initial Error/km	0	1	2	3	4	5	6	7
Estimation Error /km	4·4707	4·8165	5·1865	5·5803	5·9978	6·4371	6·8938	7·3632

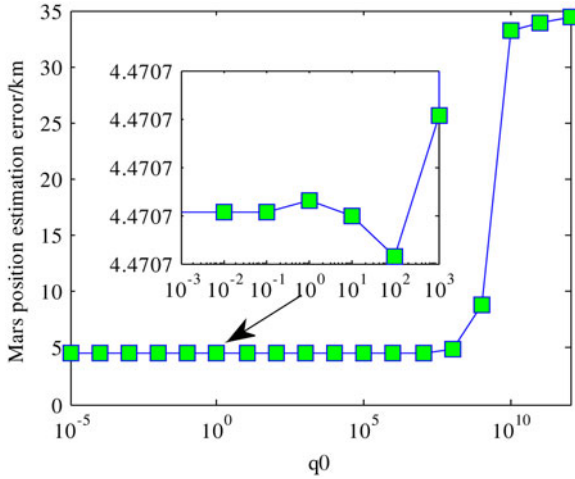


Figure 15. Impacts of the process noise covariance on the estimation error of the ephemeris uncertainty.

Table 8. Estimation accuracy with different process noise covariance matrices.

q_0	Estimation Error /km	q_0	Estimation Error /km
10^{-5}	4·4707	10^4	4·4707
10^{-4}	4·4707	10^5	4·4711
10^{-3}	4·4707	10^6	4·4742
10^{-2}	4·4707	10^7	4·5059
10^{-1}	4·4707	10^8	4·8333
10^0	4·4707	10^9	8·7871
10^1	4·4707	10^{10}	33·1153
10^2	4·4707	10^{11}	33·8097
10^3	4·4707	10^{12}	34·4143

Table 9. Estimation accuracy with different measurement noise covariance matrices.

Measurement noise covariance	Estimation Error /km
Ideal R_{err}	4·4707
Approximate R_{err}	1·1426

accurate when measurement noise covariance is the ideal one \tilde{R}_{err} . However because of the limited prior knowledge of the measurement noise, high estimation accuracy is hard to achieve.

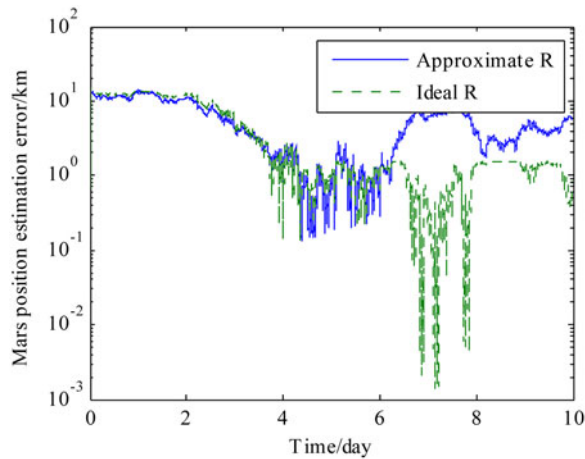


Figure 16. Impacts of the measurement noise covariance on the estimation error of the ephemeris uncertainty.

8. CONCLUSIONS. This paper has presented a Radio/Optical integrated navigation method based on ephemeris correction for a probe to approach a target planet. In this paper, the ephemeris error model is established, and the analytical solution of the ephemeris uncertainty is considered as the measurement. The target ephemeris error is estimated and fed back to modify the force models, and its accuracy impact factors are analysed.

Furthermore, based on the accurate target ephemeris uncertainty estimation and correction, the Radio/Optical integrated navigation method provides precise navigation information with respect to Earth simultaneously to that with respect to the target.

The results demonstrate that by applying the proposed method the navigation errors caused by the ephemeris uncertainty dramatically decrease and the accuracy is sufficient for a successful approach to a target.

ACKNOWLEDGMENTS

The authors would like to thank all members of Science and Technology on Inertial Laboratory and those of Fundamental Science on Novel Inertial Instrument and Navigation System Technology Laboratory for their useful comments on this work.

FINANCIAL SUPPORT

The work described in the current paper was supported by the National Science Foundation of China (grant Nos. 61233005 and No. 61004140); National Basic Research Program of China (grant No. 2014CB744202); Innovation Foundation of BUAA for PhD Graduates; New Century Program for Excellent Talents of the Ministry of Education of China; The Shanghai Committee of Science and Technology (grant No.13dz2260100) and Open Project supported by Shanghai Key Laboratory of Deep Space Exploration Technology (grant No. DS201501-002).

REFERENCES

- Acton, C. H. (1996). Ancillary Data Services of NASA's Navigation and Ancillary Information Facility. *Planetary and Space Science*, **44**, 65–70.
- Antreasian, P. G., Ardalan, S. M., Beswick, R. M., Criddle, K. E., Ionasescu, R., Jacobson, R. A., Jones, J. B., MacKenzie, R. A., Parcher, D. W., Pelletier, F. J., Roth, D. C., Thompson, P. F. and Vaughan, A. T. (2008). Orbit Determination Processes for the Navigation of the Cassini-Huygens Mission. *Proceedings of SpaceOps 2008 Conference*, Heidelberg, Germany.
- Bar-Shalom, Y., Rong, L. X. and Kirubarajan, T. (2001). *Estimation with Applications to Tracking and Navigation*. John Wiley & Sons, Inc.
- Fang, J. C. and Ning, X. L. (2010). *Methods of Autonomous Celestial Navigation for Deep Space Explorer*. North western Polytechnical University Press. (In Chinese)
- Folkner, W. M. (2010). Uncertainties in the JPL Planetary Ephemeris. *Proceedings of the Journées 2010*, Paris, France.
- Folkner, W. M., Williams, J. G. and Boggs, D. H. (2008). The planetary and lunar ephemeris DE 421. *NASA The Interplanetary Network Progress Report*, 1–31.
- Graven, P., Collions, J., Sheikh, S., Hanson, J., Ray, P. and Wood, K. (2008). XNAV for Deep Space Navigation. *Proceedings of 31st Annual AAS Guidance and Control Conference*, Breckenridge, Colorado.
- Guo, Y. P. (1999). Self-contain Autonomous Navigation System for Deep Space Missions. *Proceedings of 1999 AAS/AIAA Space Flight Mechanics Meeting*, Breckenridge, CO.
- Høg, E., Fabricius, C., Makarov, V. V., Urban, S. E., Corbin, T. E., Wycoff, G. L., Bastian, U., Schwekendiek, P. and Wicenc, A. (2000). The Tycho-2 Catalogue of the 2.5 Million Brightest Stars. *Astronomy and Astrophysics*, **355**, L27–L30.
- Jordan, J. F., Madrid, G. A. and Pease, G. E. (1972). Effects of Major Errors Sources on Planetary Spacecraft Navigation Accuracies. *Journal of Spacecraft*, **9**, 196–204.
- Julier, S. J. and Uhlmann, J. K. (1997) A New Extension of the Kalman Filter to Nonlinear Systems. *Proceedings of SPIE 3068 Signal Processing, Sensor Fusion, and Target Recognition VI*, Orlando, FL.
- Julier, S. J., Uhlmann, J. K. and Durrant-Whyte, H. F. (2000). A New Method for the Nonlinear Transformation of Means and Covariances in Filters and Estimators. *IEEE Transactions on Automatic Control*, **45**, 477–82.
- Karniely, H. and Siegelmann, H. T. (2000). Sensor Registration using Neural Networks. *IEEE Transactions on Aerospace and Electronic System*, **36**: 85–101.
- Klumpp, A. R., Bon, B. B., D'Amario, L. A., Downing, G. P., Frauenholz, R. B. and McReynolds, S. R. (1980). Automated Optical Navigation with Application to Galileo. *Proceedings of 1980 AIAA/AAS Astrodynamics Conference*, Danvers, Massachusetts.
- Lee, D. J. and Kyle, T. A. (2004). Adaptive Sigma Point Filtering for State and Parameter Estimation. *Proceedings of 2004 AIAA/AAS Astrodynamics Specialist Conference and Exhibit*, Providence, Rhode Island.
- Lemoine, F. G., Smith, D. E., Rowlands, D. D., Zuber, M. T., Neumann, G. A. and Chinn, D. S. (2001). An Improved Solution of the Gravity Field of Mars (GMM-2B) from Mars Global Surveyor. *Journal of Geophysical Research*, **106**, 23359–23376.
- Ma, X., Fang, J. C. and Ning, X. L. (2013). An Overview of the Autonomous Navigation for a Gravity-Assist Interplanetary Spacecraft. *Progress in Aerospace Sciences*, **63**, 56–66.
- Ma, X., Fang, J. C., Ning, X. L., Liu, G., Ge, S. S. (2015). Autonomous Celestial Navigation for a deep space probe approaching a target planet based on ephemeris correction. *Proceedings of IMechE Part G: Journal of Aerospace Engineering*, DOI: 10.1177/0954410015586841 (in press).
- Ma, X., Ning, X. L. and Fang, J. C. (2012) Analysis of Orbital Dynamic Equation in Navigation for a Mars Gravity-Assist Mission. *Journal of Navigation*, **65**, 531–548.
- Martin-Mur, T. J., Bhaskaran, S., Cesarone, R. J. and McElrath, T. (2008). The next 25 Years of Deep Space Navigation. *Proceedings of 2008 AAS Guidance Navigation and Control Conference*, Breckenridge, CO.
- Murrow, D. W. and Jacobson, R. A. (1988). Galilean Satellite Ephemeris Improvement using Galileo Tour Encounter Information. *Proceedings of 1988 AIAA/AAS Astrodynamics Conference*, Minneapolis, MN.
- Ning, X. L. and Fang, J. C. (2008) Spacecraft autonomous navigation using unscented particle filter-based celestial/Doppler information fusion. *Measurement Science and Technology*, **19**, 095203.

- Ning, X. L., Ma, X., Peng, C., Quan, W. and Fang, J. C. (2012b). Analysis of Filtering Methods for Satellite Autonomous Orbit Determination using Celestial and Geomagnetic Measurement. *Mathematical Problems in Engineering*, doi:10.1155/2012/267875.
- Ning, X. L., Ma, X., Zhang, X. L. and Wu, J. Y. (2012a) Autonomous Pulsars Navigation Method based on ASUKF for Mars Probe. *Journal of Beijing University of Aeronautics and Astronautics*, **38**, 22–27. (In Chinese)
- Paluszek, M. A., Mueller, J. B. and Littman, M. G. (2010). Optical Navigation System. *Proceedings of 2010 AIAA Infotech@ Aerospace*, Atlanta, Georgia.
- Payne, O. and Marrs, A. (2004). An Unscented Particle Filter for GMTI Tracking. *Proceedings of 2004 IEEE Aerospace Conference*, Big Sky, MT.
- Riedel, J. E., Owen, W. M., Stuve, J. A., Synnott, S. P. and Vaughan, R. M. (1990) Optical Navigation During the Voyager Neptune Encounter. *Proceedings of 1990 AIAA/AAS Astrodynamics Conference*, Portland.
- Rosenblatt, P., Lainey, V., Le Maistre, S., Martyc, J. C., Dehanta, V., Pätzold, M., Van Hoolst, T. and Häusler, B. (2008). Accurate Mars Express Orbits to Improve the Determination of the Mass and Ephemeris of the Martian Moons. *Planetary and Space Science*, **56**, 1043–1053.
- Rourke, K. H., Acton, C. H., Breckenridge, W. G., Campbell, J. K., Christensen, C. S., Donegan, A. J., Jerath, N., Mottinger, N. A., Rinker, G. C. and Winn, F. B. (1977). The Determination of the Interplanetary Orbits of Vikings 1 and 2. *Proceedings of AIAA 15th Aerospace Sciences Meeting*, Los Angeles, Calif.
- Thornton, C. L. and Border, J. S. (2003). *Radiometric Tracking Techniques for Deep-Space Navigation*. John Wiley & Sons, Inc.
- Vallado, D. A. (2007). *Fundamentals of Astrodynamics and Applications*. Springer.
- van der Merwe, R., Doucet, A., de Freitas, N. and Wan, E. (2000). The Unscented Particle Filter. *Proceedings of Neural Information Processing Systems 2000*, Denver, Colorado.
- Wang, D. Y., Huang, X. Y. and Guan, Y. F. (2008). GNC System Scheme for Lunar Soft Landing Spacecraft. *Advances in Space Research*, **42**, 379–385.
- Wang, Y. D., Zheng, W., Sun, S. M. and Li, L. (2013) X-ray Pulsar-based Navigation System with the Errors in the Planetary Ephemerides for Earth-orbiting Satellite. *Advances in Space Research*, **51**, 2394–2404.
- Wood, K. S., Mowalski, M., Lovellette, M. N., Ray, P. S., Wolff, M. T., Yentis, D. J., Bandyopadhyay, R. M., Fewtrell, G., Fritz, G. M., Wood, D. and Hertz, P. L. (2001). The Unconventional Stellar Aspect (USA) Experiment on ARGOS. *Proceedings of AIAA Space 2001 Conference and Exposition*, Albuquerque, NM.
- Wu, W. R., Wang, D. Y. and Ning, X. L. (2011) *Principles and Technologies of Autonomous Navigation For a Deep Space Explorer*. China Astronautic Publishing House. (In Chinese)
- Yim, J. R., Crassidis, J. L. and Junkins, J. L. (2000) Autonomous Orbit Navigation of Interplanetary Spacecraft. *Proceedings of 2000 AIAA/AAS Astrodynamics Specialist Conference*, Denver, CO.
- Zhou, Y. F., Leung, H. and Blanchette, M. (1999). Sensor Alignment with Earth-centered Earth-fixed (ECEF) Coordinate System. *IEEE Transactions on Aerospace and Electronic Systems*, **35**, 410–418.